TESCAN

TESCAN micro-CT solutions for energy storage materials research

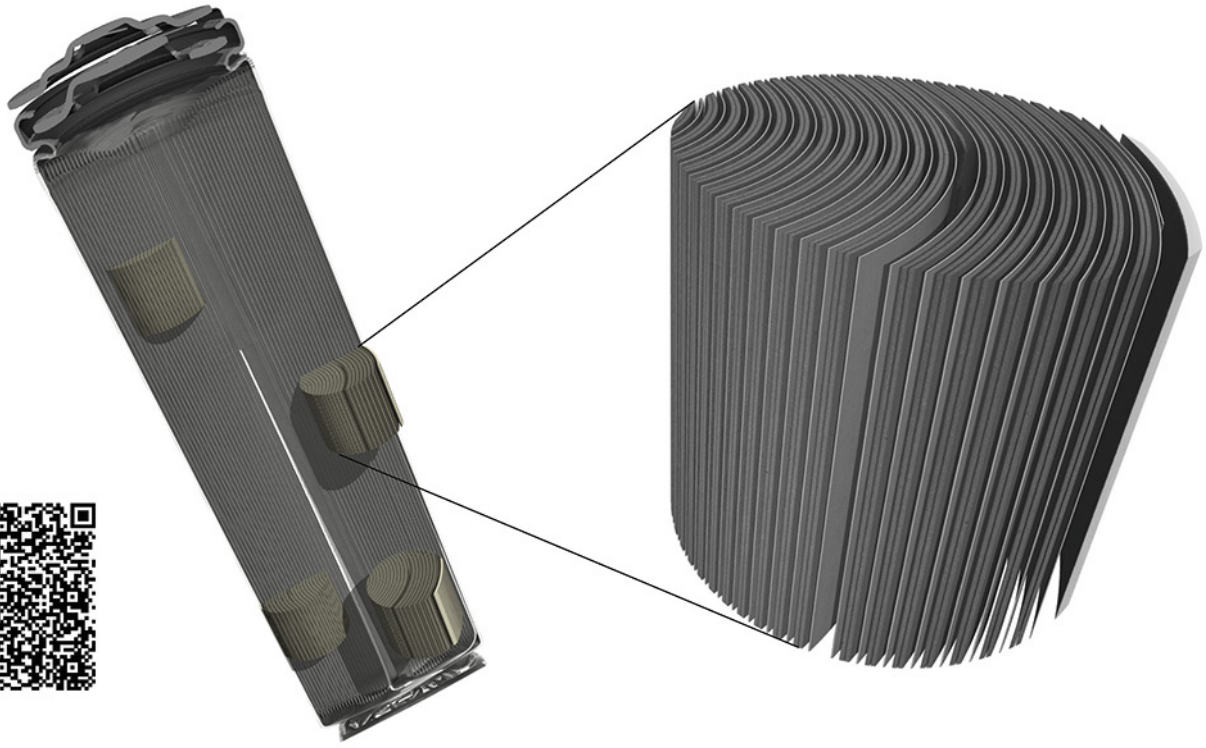

TESCAN UniTOM XL

- ✓ Multi-scale non-destructive 3D imaging optimized to maximize throughput and contrast
- ✓ Fast scanning and high sample throughput with temporal resolutions below 10 seconds
- ✓ Wide array of samples types
- ✓ Enables dynamic tomography and *in-situ* experiments
- ✓ Dynamic screening for synchrotron beamtime
- ✓ Modular and open system with unmatched flexibility for research

Click and find out more

ADVANCED ENERGY MATERIALS
www.advenergymat.de

Unveiling the Intricate Intercalation Mechanism in Manganese Sesquioxide as Positive Electrode in Aqueous Zn-Metal Battery

Yuan Ma, Yanjiao Ma, Thomas Diemant, Kecheng Cao, Xu Liu, Ute Kaiser, R. Jürgen Behm, Alberto Varzi, and Stefano Passerini**

In the family of Zn/manganese oxide batteries with mild aqueous electrolytes, cubic α-Mn_2O_3 with bixbyite structure is rarely considered, because of the lack of the tunnel and/or layered structure that are usually believed to be indispensable for the incorporation of Zn ions. In this work, the charge storage mechanism of α-Mn_2O_3 is systematically and comprehensively investigated. It is demonstrated that the electrochemically induced irreversible phase transition from α-Mn_2O_3 to layered-typed L-Zn_xMnO_2, coupled with the dissolution of Mn^{2+} and OH^- into the electrolyte, allows for the subsequent reversible de-/intercalation of Zn^{2+}. Moreover, it is proven that α-Mn_2O_3 is not a host for H^+. Instead, the MnO_2 formed from L-Zn_xMnO_2 and the Mn^{2+} in the electrolyte upon the initial charge is the host for H^+. Based on this electrode mechanism, combined with fabricating hierarchically structured mesoporous α-Mn_2O_3 microrod array material, an unprecedented rate capability with 103 mAh g^{-1} at 5.0 A g^{-1} as well as an appealing stability of 2000 cycles (at 2.0 A g^{-1}) with a capacity decay of only ≈0.009% per-cycle are obtained.

1. Introduction

Low-cost aqueous rechargeable batteries are drawing tremendous attention for application in large-scale energy storage.[1,2] By employing water-based solutions as electrolytes, this class of batteries holds great potential to effectively reduce safety and environmental issues, which are generally caused by organic electrolytes due to their often toxic, volatile, and flammable nature.[1,3] Among them, zinc-based batteries, using neutral or mild-acidic aqueous electrolytes, stand out due to the several main advantages of Zn anodes, including i) the ultrahigh theoretical volumetric capacity (5851 mAh cm^{-3} for Zn metal),[1,4] ii) the low redox potential (≈0.76 V versus standard hydrogen electrode),[5] and iii) the natural abundance and non-toxicity.[1] Importantly, Zn anodes show a promising electrochemical Zn^{2+}/Zn reversibility in aqueous electrolyte, owing to the inhibition of the H_2 evolution reaction.[1,5,6] However, to enable large-scale energy storage devices with Zn metal anodes, appropriate positive electrode materials are needed, which is the topic of this manuscript.[1,3,5]

To date, studies of host materials for positive electrodes mainly focused on Prussian blue analogs, vanadium-based compounds, polyanionic compounds, and manganese-based oxides.[1,3] Among them, Mn-based oxides (i.e., MnO_2, Mn_2O_3, Mn_3O_4, and MnO) in rechargeable aqueous zinc-metal batteries (AZMBs) attracted considerable interest, due to their low cost, non-toxicity, and abundance.[7] In addition, the high operating potential (≈1.4 V versus Zn^{2+}/Zn) and large discharge capacity further render Mn-based oxides very promising for high energy AZMBs.[1,3,8] Despite all progress, Zn/MnO_z ($1 \le z \le 2$) batteries still suffer from several issues. Furthermore, the charge storage mechanism is still highly controversial.[1,3] In this battery chemistry, in fact, not only Zn^{2+} ions can serve as cationic charge carriers, but also protons and even Mn^{2+} dissolved from the cathode. Alongside, various parasitic side reactions can occur, thereby leading to complicated electrochemical reactions.[1,3] So far, mainly three different energy storage mechanisms have been proposed to occur in aqueous Zn-MnO_z ($1 \le z \le 2$) cells: i) the reversible uptake/removal of Zn^{2+}, ii) the reaction of protons coupled with the formation of zinc hydroxide sulfate (when

Y. Ma, Y.-J. Ma, X. Liu, R. J. Behm, A. Varzi, S. Passerini
Helmholtz Institute Ulm (HIU)
Helmholtzstrasse 11, Ulm 89081, Germany
E-mail: alberto.varzi@kit.edu; stefano.passerini@kit.edu
Y. Ma, Y.-J. Ma, X. Liu, A. Varzi, S. Passerini
Karlsruhe Institute of Technology (KIT)
P.O. Box 3640, Karlsruhe 76021, Germany
T. Diemant, R. J. Behm
Institute of Surface Chemistry and Catalysis
Ulm University
Albert-Einstein-Allee 47, Ulm 89081, Germany
K.-C. Cao, U. Kaiser
Central Facility for Electron Microscopy
Group of Electron Microscopy of Materials Science
Ulm University
Albert-Einstein-Allee 11, Ulm 89081, Germany
The ORCID identification number(s) for the author(s) of this article can be found under https://doi.org/10.1002/aenm.202100962.

DOI: 10.1002/aenm.202100962

using $ZnSO_4$-based solution as electrolyte), and iii) the successive de-/intercalation of both Zn^{2+} and H^+.[6,8] However, the proposed mechanisms are not complete and still under debate since they cannot fully describe the electrochemical behavior of MnO_z ($1 \le z \le 2$) cathodes in AZMBs, especially for low-valence Mn-based oxides such as α-Mn_2O_3.[1,3] In fact, due to the absence of tunnel structures and/or widely spaced layers in the crystalline structure, α-Mn_2O_3 was considered to be electrochemically inactive for Zn^{2+} storage.[1,9,10] In contrast, very recent reports have shown that aqueous Zn/α-Mn_2O_3 cells can offer promising electrochemical performance.[11–14] This indicates that in-depth understanding of the charge storage mechanism of α-Mn_2O_3 cathodes in AZMBs must be urgently reconsidered.

In this regard, we systematically and comprehensively investigated the electrochemical behavior of α-Mn_2O_3 cathodes in AZMBs upon repeated dis-/charging process. Herein, a well-defined hierarchical mesoporous α-Mn_2O_3 (denoted as m-α-Mn_2O_3) is developed and employed as model cathode material. In fact, based on previous reports, the presence of meso-porosity can positively influence the electrochemical performance.[13,15] We found that α-Mn_2O_3 undergoes an electrochemically induced irreversible phase transition in the first cycle, resulting in a different electrochemical behavior in the following cycles. The charge storage during the following cycles mainly originates from sequential Zn^{2+} and H^+ intercalation and the dissolution-deposition of Mn^{2+}. Besides the study of the electrode mechanism, owing to the unique hierarchical mesoporous structure, m-α-Mn_2O_3 cathodes also showed appealing electrochemical properties in AZMBs with excellent rate capability and long-term cycle lifespan.

2. Results and Discussion

Starting from a manganese-based metal organic framework (Mn-MOF) with terephthalic acid as the organic ligand,[16] hierarchical m-α-Mn_2O_3 microrods were synthesized via a simple calcination at 600 °C in air (**Figure 1**a), which is described in more detail in the Experimental Section. Note that the annealing temperature (i.e., 600 °C) was selected based on the control experiments presented in Figure S1, Supporting Information. The Rietveld refinement of the powder X-ray diffraction (XRD) pattern of the resulting product (Figure 1b) indicates that all reflections can be explained by the bixbyite-type α-Mn_2O_3 cubic phase (space group:

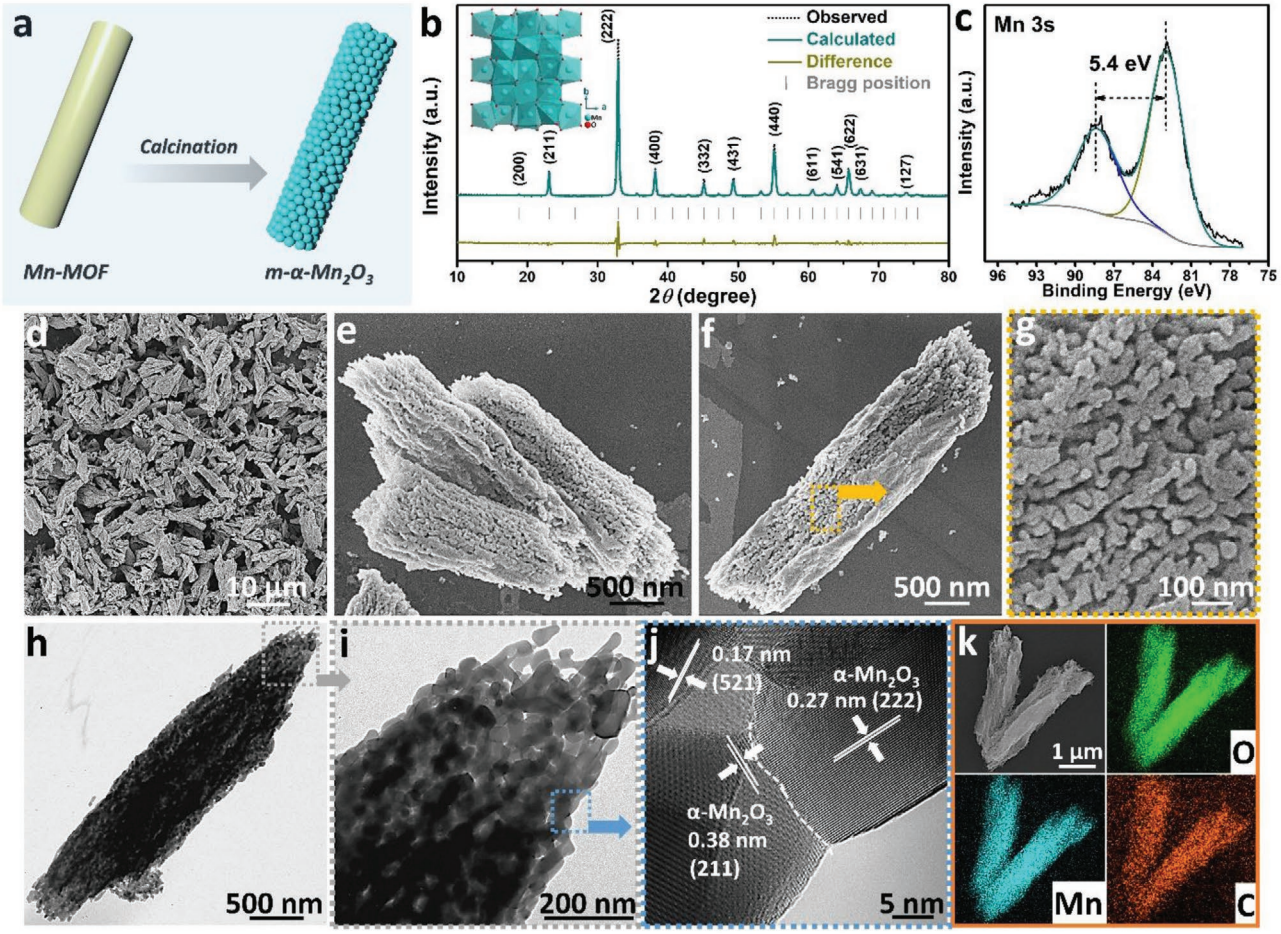

Figure 1. a) Schematic illustration of the synthesis process used to prepare hierarchical m-α-Mn_2O_3 microrods via calcination of the Mn-MOF template in air. b) Powder XRD pattern and the Rietveld refinement of m-α-Mn_2O_3. The inset displays the crystal structure model projected along [001]. c) High-resolution XP spectrum in the Mn 3s region of m-α-Mn_2O_3. Morphological and structural characteristics of hierarchical m-α-Mn_2O_3 microrods: d–g) SEM and h,i) TEM images with different magnifications; j) HRTEM micrograph; and k) EDX elemental mapping images.

Ia-3m [206], crystallography open database #96-151-4238, cf. inset in Figure 1b) with lattice parameters of a = b = c = 9.41221 Å and a cell volume = 833.824 Å^3. The crystal structure refinement was performed with satisfactory agreement factors (R_{wp} = 4.98%, R_p = 3.42%).[17] Also, no unexpected diffraction peaks from impurities were observed in the XRD pattern.

X-ray photoelectron spectroscopy (XPS) was used to characterize the surface composition and oxidation state of the as-prepared m-α-Mn_2O_3 sample. The XPS survey spectrum (Figure S2, Supporting Information) shows the presence of Mn, O, and C in the as-obtained m-α-Mn_2O_3 in the surface region, and no other elements. The C 1s peak can be assigned to carbon surface impurities on the m-α-Mn_2O_3 surface, probably due to residuals of organic ligands and contamination during transport in air. In fact, the overall C content, determined via thermogravimetric analysis (TGA), is only ≈3 wt% (Figure S3, Supporting Information). The Mn 2p high-resolution spectrum (Figure S4, Supporting Information) displays the Mn 2p peak doublet with the Mn $2p_{3/2}$ and $2p_{1/2}$ peaks located at around 641.9 and 653.5 eV, respectively, which indicates the presence of Mn^{3+} in the resulting product.[18,19] To identify the oxidation state of Mn more clearly, a detailed spectrum in the region of the Mn 3s peak was also acquired and analyzed (Figure 1c). Since the extent of the Mn 3s multiplet splitting is known to decrease along with an increased valence of Mn, that is, from ≈6 eV for Mn^{2+} to ≈5.3 eV for Mn^{3+} and ≈4.7 eV for Mn^{4+},[16] the splitting of 5.4 eV detected in Figure 1c confirms the Mn^{3+} valence in m-α-Mn_2O_3. Hence, the Mn-MOF precursor was successfully converted into α-Mn_2O_3 via a simple calcination process, despite the presence of some C-based residues.

The morphological and structural features of the m-α-Mn_2O_3 microrods were investigated in detail by scanning electron microscopy (SEM), transmission electron microscopy (TEM), and high-resolution TEM (HRTEM). The overview (Figure 1d) and enlarged (Figure 1e) SEM images reveal that the m-α-Mn_2O_3 microrods are quite homogeneous, with lengths and widths of ≈2–3 µm and around 1 µm, respectively. Owing to the mild, calcination process, the final product still displays the original shape of the parental Mn-MOF particles.[16] A closer look at high magnification (see Figure 1f,g) reveals that the surface of m-α-Mn_2O_3 is relatively rough, showing numerous small and randomly distributed meso- and macropores (Figure 1g). The results of the TEM analysis are displayed in Figure 1h–j. A well-defined porous structure could be recognized in the low-magnification TEM image in Figure 1h. It was pointed out before that the porous structure most probably results from the release of gaseous products (e.g., CO_2, H_2O, and CO) generated from the Mn-MOF precursor during the calcination process.[16,20] The high-magnification TEM in Figure 1i shows that the microrod structure is formed by the short-range ordered aggregation of nanoparticles with an average size of 25 nm. The HRTEM image in Figure 1j reveals that α-Mn_2O_3 nanoparticles are in tight contact with each other, forming nano-interfaces between them. In agreement with the XRD results, we find three sets of obvious lattice fringes with d-spacings of 0.38, 0.27, and 0.17 nm, which can be assigned to the (211), (222), and (521) plane of α-Mn_2O_3, respectively (Figure 1j). Figure 1k finally shows energy-dispersive X-ray spectroscopy (EDX) elemental mapping images of two m-α-Mn_2O_3 microrods, displaying the uniform distribution of Mn and O coupled with residual C throughout the entire nanostructured particles.

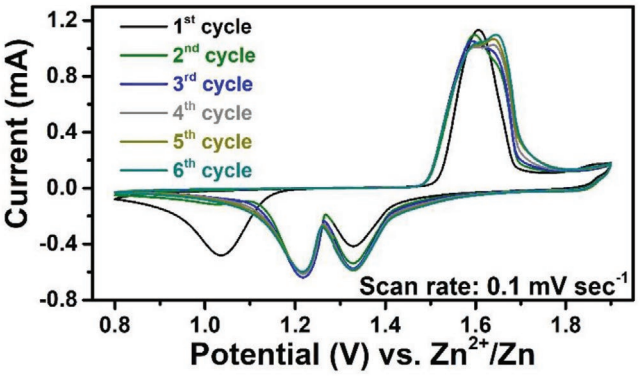

Figure 2. Cyclic voltammograms of a Zn/m-α-Mn_2O_3 cell employing the 3.0 M $ZnSO_4$ and 0.2 M $MnSO_4$ solution as electrolyte, recorded at a scan rate of 0.1 mV s^{-1} from 0.8 to 1.9 V.

The porous character of the resulting product was further probed by N_2 adsorption isotherms at 77 K (Figure S5, Supporting Information). The material features a moderate specific Brunauer–Emmett–Teller (BET) surface area of 56.8 m^2 g^{-1}, which is substantially higher than that of commercial α-Mn_2O_3 (denoted as b-α-Mn_2O_3). The pore size distribution of m-α-Mn_2O_3, determined using the Barrett–Joyner–Halenda (BJH) method (Figure S5b, Supporting Information), is centered around 20 nm, confirming that m-α-Mn_2O_3 possesses a mesoporous character. Such a mesoporous structure built by ultrafine primary nanoparticles provides sufficient surface area to promote electrochemical reactions and efficient penetration of the electrolyte into the active material.[16,21]

The electrochemical behavior of m-α-Mn_2O_3 as positive electrode (cathode) in Zn metal battery was investigated in an aqueous electrolyte containing 3.0 mol L^{-1} (3.0 M) $ZnSO_4$ and 0.2 mol L^{-1} (0.2 M) $MnSO_4$. Note that each cell contains 90 µL of electrolyte. According to previous literature, the addition of $MnSO_4$ in the aqueous electrolyte has several positive effects, including an extended cycling lifespan (a detailed discussion is given later) and an improved Zn^{2+} plating/stripping performance.[22–24] The cyclic voltammogram of a Zn/m-α-Mn_2O_3 cell (**Figure 2**) reveals characteristics similar that of a Zn/b-α-Mn_2O_3 cell (Figure S6, Supporting Information). In the initial sweep, an obvious cathodic peak located at ≈1.03 V is observed, while a sharp anodic peak appears at ≈1.60 V. In the following sweeps, however, we observed a substantially different current response, suggesting a significant structural reorganization during the first cycle.[9] Hence, the initial cycle induces an electrochemical activation of the α-Mn_2O_3. In the following cycles, two new cathodic peaks are observed at ≈1.33 and 1.22 V, respectively, coupled with the gradual disappearance of the original cathodic peak at ≈1.03 V. The anodic peak almost maintains its original position (≈1.60 V), but with the gradual evolution of a new shoulder at ≈1.64 V. These two couples of redox peaks were previously assigned to the stepwise electrochemical de-/insertion of H^+ and Zn^{2+}.[12,22] As demonstrated in the following, however, this explanation is not completely appropriate for the present α-Mn_2O_3 system.

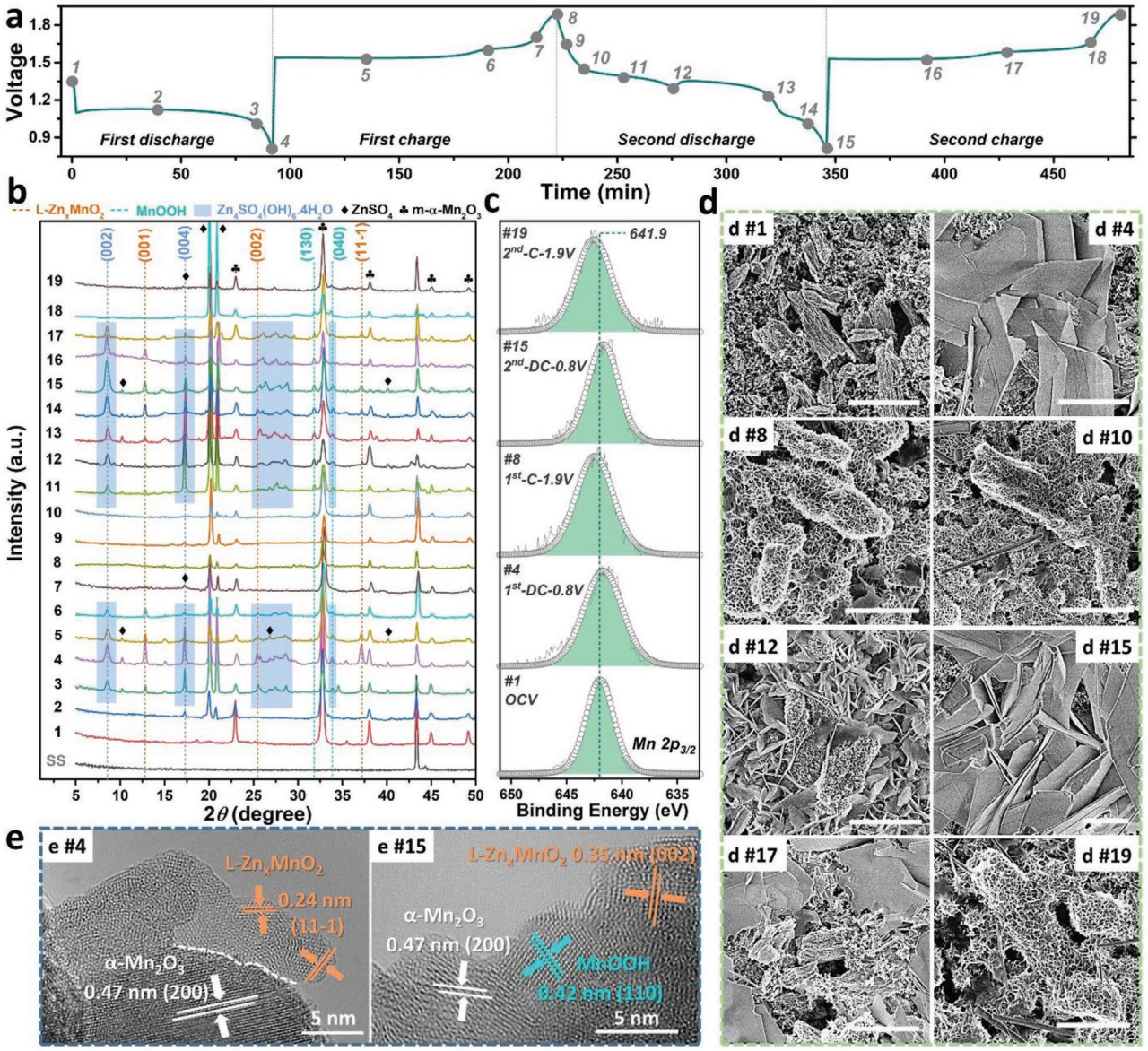

Figure 3. Characterization of the structural evolution of m-α-Mn_2O_3 upon cycling of the Zn/m-α-Mn_2O_3 battery. a) Typical dis-/charge voltage profiles for the initial two cycles at 100 mA g^{-1}. The numbers from 1 to 19 mark the state of charge of the various samples used to perform ex situ XRD, XPS, SEM, and TEM analysis. b) Evolution of the ex situ XRD patterns of m-α-Mn_2O_3 collected at different states of charge (from #1 to #19), SS = Stainless-steel. c) Ex situ XPS detail spectra of the Mn $2p_{3/2}$ region of the pristine (#1), first fully discharged (#4), first fully charged (#8), second fully discharged (#15), and second fully charged (#19) samples. d) SEM images illustrating the morphologic evolution occurring in the electrodes at different states of charge (#1, #4, #8, #10, #12, #15, #17, and #19, scale bars: 1 µm). e) Ex situ HRTEM images of the samples in the first (#4) and second (#15) fully discharged state.

Several Zn/m-α-Mn_2O_3 batteries were realized, see **Figure 3**; Figures S7–S20 and Tables S1,S2, Supporting Information, to perform a combination of various post-mortem and operando analysis investigations, to characterize the structural and chemical properties of m-α-Mn_2O_3 electrodes at different states of charge during the initial (two) galvanostatic dis-/charge cycles. This extensive investigation included the use of different electrolytes. Figure 3 displays data obtained using a 3.0 M $ZnSO_4$ + 0.2 M $MnSO_4$ aqueous solution as electrolyte. To avoid electrode contamination, all cycled cells were disassembled in an argon-filled glovebox (more details in the Experimental Section). The dis-/charge profiles for the first two cycles, which are presented in Figure 3a, illustrate the selected states of charge (highlighted by grey points) for the comprehensive ex situ analysis to investigate the detailed reaction mechanism.

In the first discharge, a long plateau from open circuit voltage to 0.8 V is observed (Figure 3a) corresponding to the cathodic peak at ≈1.03 V in the first cyclic voltammetry (CV) curve (Figure 2). The related XRD patterns (#1 → #4, Figure 3b) reveal a pronounced decrease in the intensity of the main α-Mn_2O_3 reflections, accompanied by the simultaneous appearance of several new peaks. More precisely, two new phases can be discerned. The first phase is associated with three new reflections

gradually evolving at 12.7°, 25.4°, and 37.2°, which match with layered-type L-Zn_xMnO_2 (JCPDS card no. 42-1317, see Figure S7, Supporting Information).[11,25] Apparently, part of the α-Mn_2O_3 undergoes a phase transformation upon reduction of Mn (III) to Mn (II). A similar transformation of structure and oxidation state was also observed by in situ XRD experiments for the Zn/γ-MnO_2 system.[25] They revealed that γ-MnO_2 (Mn (IV)) was stepwise reduced to eventually Mn (II) upon Zn^{2+} intercalation. More precisely, $ZnMn(III)_2O_4$ was formed in the early stage of the evolution followed by its further transformation into two different Mn (II)-phases, that is, L-Zn_xMnO_2 and γ-Zn_yMnO_2. Note that γ-Zn_yMnO_2 stems from the 1×2 tunnel structures of the parent γ-MnO_2 which are occupied by Zn^{2+}. In our case, however, L-Zn_xMnO_2 is directly obtained from trivalent α-Mn_2O_3, undergoing a single-step phase transition process. Ex situ XPS and TEM in Figure 3c,e provide further evidence for this phase transformation in the first discharge and the concomitant change of the Mn oxidation state. Before discussing the XPS results, it may be noted that the analysis of the Mn 3s multiplet split used to confirm the oxidation state of Mn (III) in m-α-Mn_2O_3 powder is not suitable for the characterization of Zn-containing electrodes because of the appearance of the Zn 3p peak in the same region. Instead, the Mn $2p_{3/2}$ region (the Mn $2p_{1/2}$ region is also affected by a Zn feature) was used. However, the further deconvolution of the spectra in this region is hardly possible since the multiplet splitting of Mn (II) to Mn (IV) results in rather complex peak assemblies. The XP spectrum in the Mn $2p_{3/2}$ region of the pristine electrode (Figure 3c, #1) is dominated by a peak at ≈641.9 eV, which can be assigned to Mn^{3+} in m-α-Mn_2O_3.[26,27] The spectrum after the first discharge to 0.8 V (Figure 3c, #4) shows a slight shift of the peak maximum toward lower binding energy (≈641.6 eV), together with a broadening of the peak to lower binding energies, indicating a partial reduction of Mn^{3+} to Mn^{2+} upon Zn^{2+} insertion.[26,28] Furthermore, the ex situ TEM image (Figure 3e, #4) of the sample in the fully discharged state reveals that several crystalline grains form on the surface of the α-Mn_2O_3 particles. The observed lattice fringes with an interplanar distance of 0.24 nm can be assigned to the (11-1) plane of L-Zn_xMnO_2, corroborating the intercalation of Zn^{2+}. The XRD patterns recorded during the first discharge (Figure 3b) also display reflections of a second new phase, which develops starting from #3. These features appearing at 8.5°, 33.8°, and in the 25.1–29.5° range (highlighted by blue color) match with those of $Zn_4SO_4(OH)_6 \cdot 4H_2O$ (zinc hydroxide sulfate hydrate (ZHSH), JCPDS card no. 44-0673, see Figure S7, Supporting Information, taking into account that some reflections overlapped with those of $ZnSO_4$ (at ≈17° and ≈21°, Figure 3b and Figure S8, Supporting Information)). The evolution of the morphology of the electrode surface was characterized by ex situ SEM imaging (Figure 3d). Large 2D flake-shaped crystals appear at the fully discharged state (Figure 3d, #4). EDX analysis (Figure S9, Supporting Information) demonstrates that the flakes mainly contain Zn, S, and O with only trace amounts of Mn, indicating these flakes to be ZHSH. As expected, Mn is mainly concentrated in the m-α-Mn_2O_3 microrods. Furthermore, EDX elemental mapping images also reveal that the appearance of Zn signals and the concomitant absence of S signals on the surface of the microrods, once more indicating the intercalation of Zn to occur into the m-α-Mn_2O_3 host. Notably, the formation of ZHSH is commonly observed in Zn/MnO_2 cells.[24] Specifically, MnO_2 can react with a proton from the water to generate MnOOH, resulting in a rapid increase of the OH^- concentration in the vicinity of the electrode, which in turn leads to the precipitation of flake-like ZHSH on the electrode surface. In our case, the pH value of the electrolyte indeed increases at the end of the first discharge (Table S1, Supporting Information). However, the initial discharge capacity of Zn/m-α-Mn_2O_3 battery in 0.2 M $MnSO_4$ is close to 0 mAh g^{-1} (Figure S10, Supporting Information), indicating that m-α-Mn_2O_3 does not react extensively with H^+. To further confirm this evidence, a Zn/m-α-Mn_2O_3 cell employing the 3.5 M $MnSO_4$ electrolyte was subjected to discharge. Although its pH value is close to that of the 3.0 M $ZnSO_4$ + 0.2 M $MnSO_4$ electrolyte, the cell delivers a negligible capacity as well (Figure S11, Supporting Information). Therefore, we speculate that the OH^- may derive from the structural transformation process of m-α-Mn_2O_3 during Zn^{2+} insertion rather than from H^+ insertion. This means that H_2O is involved in the phase transformation. This is further confirmed by the fact that only a poor capacity is delivered in organic electrolyte (3.0 M $ZnSO_4$ in dimethyl sulfoxide (DMSO) solution) due to the absence of H_2O (see Figure S12, Supporting Information).

In the following (first) charge (#4 → #8), XRD patterns (Figure 3b) reveal a continuous decrease of the L-Zn_xMnO_2 reflections, eventually disappearing in #8, which indicates the deintercalation of Zn upon recharging. A similar intensity evolution of the (00*l*) reflections has been observed for layered intercalation electrodes such as vanadium oxides.[29,30] Meanwhile, the features of ZHSH, that is, the diffraction peaks and the flake-shaped morphology, both disappear in the XRD patterns (Figure 3b, #7 & #8) and in the SEM image (Figure 3d, #8), respectively (the related reason will be discussed later).

The data clearly indicate that the specific capacity during the first charge is higher than in the previous discharge process. An explanation for this behavior can be found in the XP spectrum of the fully recharged electrode (Figure 3c, #8), which shows a shift of the Mn $2p_{3/2}$ peak maximum to higher binding energy, beyond that of the pristine state of Mn (III). This suggests that Mn (IV) is formed upon recharging the cell. Interestingly, no related features could be identified in the XRD pattern at points #7/#8 (Figure 3b), indicating the formation of (quasi)amorphous Mn(IV)-based compounds on the (near) surface region of the electrode.[27,28] Furthermore, the ex situ SEM image of the electrode after the first recharge (Figure 3d, #8) displays new interconnected porous layers on the cathode material surface. Ex situ SEM and XRD measurements (Figure S13, Supporting Information) show that such an interconnected porous layer, also formed on the bare current collector, is composed of layered birnessite-MnO_2, which probably forms by the oxidation of Mn^{2+} ion from the electrolyte. Actually, this process could be responsible for the extra charge capacity observed during the first charge ($C_{charge} > C_{discharge}$).[9,23] Interestingly, the oxidation process of Mn^{2+} involves the formation of H^+ in the electrolyte (Table S1, Supporting Information with related discussion), which leads to the dissolution of the flake-like ZHSH.

To further deepen our understanding of the abovementioned additional capacity during the first charge ($C_{charge} > C_{discharge}$), additional measurements were carried out testing Zn/m-α-Mn_2O_3 batteries with two other electrolytes, that is,

3.0 M $ZnSO_4$ or 0.2 M $MnSO_4$. For the latter electrolyte, the results shown in Figure S10, Supporting Information prove the oxidation of Mn^{2+} from the electrolyte as a possible reason for the additional charge capacity. In fact, the voltage profile of the Zn/m-α-Mn_2O_3 battery employing the 0.2 M $MnSO_4$ electrolyte confirms that although no capacity is delivered during the first discharge, a specific capacity of ≈28 mAh g^{-1} is obtained upon fully recharging (Figure S10, Supporting Information). This is coupled with the formation of interconnected porous layers on the electrode surface as revealed by ex situ SEM imaging (Figure S14a, Supporting Information). Interesting, however, the extra charge capacity is observed also when using the 3.0 M $ZnSO_4$ electrolyte (Figure S10, Supporting Information), in spite of the absence of Mn^{2+} in the electrolyte. There are two potential causes for this: i) α-Mn_2O_3 is oxidized to Mn(IV) compounds or ii) Mn^{2+} is dissolved in the electrolyte upon Zn^{2+} insertion in the discharge and then re-oxidized to form Mn(IV) compounds upon recharging coupled with offering extra electrons. We lean toward the latter interpretation, owing to the formation of the interconnected porous birnessite layer (ex situ SEM in Figure S14b, Supporting Information). Furthermore, an electrochemical experiment in which a Zn/3.0 M $ZnSO_4$/m-α-Mn_2O_3 cell was first charged to 1.9 V and then discharged to 0.8 V, was performed to confirm our second hypothesis (Figure S15, Supporting Information). As can be seen, no capacity is obtained during charge, while the subsequent discharge process shows an electrochemical behavior analogous as the initially discharged cells (compare Figures S10 and S15, Supporting Information). This indicates that the formation of Mn^{2+} upon discharge and its dissolution are not only the basis for the birnessite layer formation, but are also a necessary activation process for the m-α-Mn_2O_3 (and b-α-Mn_2O_3) electrodes to become active for Zn^{2+} insertion in the following cycles. Importantly, the dissolution of Mn^{2+} in the electrolyte with 3.0 M $ZnSO_4$ upon discharging to 0.8 V was also proved by ex situ inductively coupled plasma optical emission spectroscopy (ICP-OES) analysis (see Table S2, Supporting Information, with related discussion).

Based on these findings, we propose a comprehensive set of reactions for explaining the overall charge-/discharge process in the Zn/m-α-Mn_2O_3 cell (see **Figure 4**a). During the first discharge, α-Mn_2O_3 undergoes Zn insertion to form layered L-Zn_xMnO_2 $_{(0.5 < x \leq 1)}$ along with Mn^{2+} and OH^- dissolution in the electrolyte. The generated OH^- reacts with $ZnSO_4$ and H_2O to form flake-like ZHSH. In the subsequent charge process, the capacity is mainly determined by i) the Zn deinsertion from L-Zn_xMnO_2 $_{(0.5 < x \leq 1)}$, and ii) the electrochemical deposition (oxidization) of Mn^{2+} to generate birnessite-MnO_2. The deposition process produces H^+, causing the dissolution of ZHSH. Based on the electrochemical reactions during the first cycle, the theoretical specific capacity of α-Mn_2O_3 can be calculated to be ≈339.4 mAh g^{-1} upon discharge and ≈678.7 mAh g^{-1} upon charge (see discussion with Table S2, Supporting Information). The resulting material features a potential and cycling stability that makes it a highly appealing cathode material for AZMBs, although the high theoretical

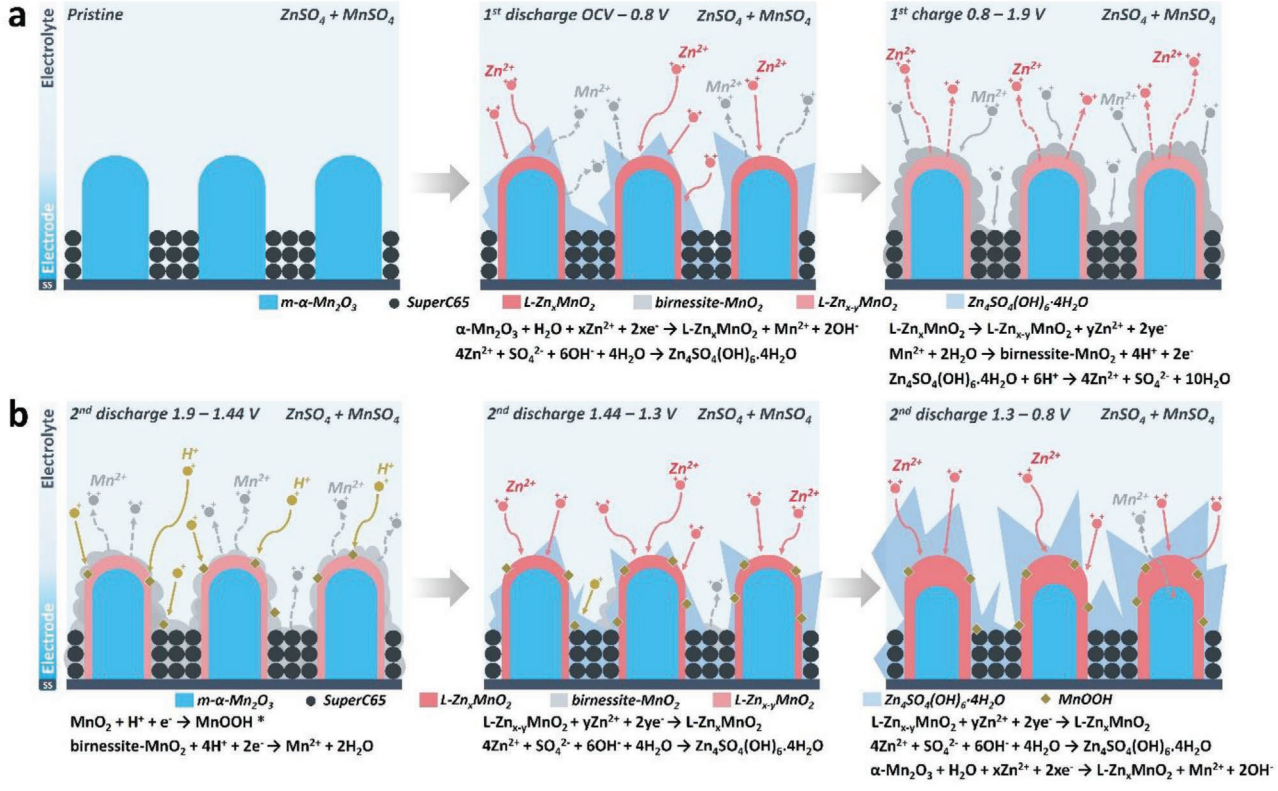

Figure 4. Schematic illustration illustrating the different contributions to the charge storage mechanism of m-α-Mn_2O_3-based AZMBs during a) the first discharge and charge process and b) the second discharge process. *MnO_2 contains birnessite-MnO_2 and L-$Zn_{x-y}MnO_2$ (when $x-y=0$).

capacities were not achieved in this work (see discussion with Figure S16, Supporting Information).

In the second cycle, the Zn/m-α-Mn_2O_3 battery shows a rather different voltage profile, especially with regard to the discharge process (Figure 3a). Differences are also evidenced by the ex situ XRD patterns (Figure 3b, from #8 to #19). The reflections related to L-Zn_xMnO_2 and ZHSH both appear in the pattern at #11 (≈1.39 V), that is, at a higher potential than in the first discharge process (≈1.0 V). With respect to L-Zn_xMnO_2, this can be ascribed to the different host material at the beginning of the discharge, that is, α-Mn_2O_3 for the first cycle, but L-$Zn_{x-y}MnO_2$ $_{(0.5 < x \leq 1;\ 0.5 \leq y \leq 1)}$ for the second cycle. However, this difference for ZHSH probably originates from its different formation mechanism between the first and second cycles. The intensity of the L-Zn_xMnO_2 and ZHSH reflections in the XRD patterns continuously increases until complete discharge (#15), while the reverse behavior is recorded upon recharging (#15 → #19). Meanwhile, the XPS data (Figure 3c, #8, #15, and #19) demonstrate the evolution of the Mn oxidation state during the second cycle. Upon discharge to 0.8 V, the Mn $2p_{3/2}$ signal shifts to lower binding energy (even below that of the pristine material), indicating the reappearance of Mn^{2+} due to Zn^{2+} intercalation (#15), whereas the spectrum at 1.9 V (#19, fully charged) recovers a shape similar to that at the beginning of the second cycle (#8). The structural evolution of ZHSH during the second cycle is also testified by the ex situ SEM images (Figure 3d, #8 → #19). The 2D flake-shaped particles gradually form on the electrode surface during the second discharge (#8 → #15), and disappear in the following charge (#15 → #19). The high reversibility of the deposition and dissolution of ZHSH flakes during the dis-/charge process is in agreement with the structural evolution observed in the XRD patterns.

Importantly, the XRD patterns recorded during the second cycle (Figure 3b) show the appearance of a new feature at 31.7° during discharge (from #8 to #15), which declines again upon recharge to completely vanish at the end of the cycle (from #15 to #19). This reflection, observed for the first time upon discharge to ≈1.45 V (#10), is assigned to the (130) plane of MnOOH (JCPDS card no. 24-0317, see Figure S7, Supporting Information).[10,31] Note that other typical reflections of MnOOH, that is, located at ≈21.2° ((110) plane), ≈33.5° ((040) plane), and ≈38° ((111) plane), overlapped with those of $ZnSO_4$ (at ≈21°), ZHSH (at ≈33.8°), and α-Mn_2O_3 (at ≈38.2°, see Figure 3b and Figures S7 and S8, Supporting Information), respectively. Based on the previous discussion, the formation of MnOOH stems from the reaction of Mn(IV)O_2 (i.e., L-$Zn_{x-y}MnO_2$ (when $x-y$ is 0) and/or birnessite-MnO_2) with protons from water. Apart from XRD, findings from ex situ TEM further verify the formation of MnOOH. The TEM image of an electrode at the (second) fully discharged state (Figure 3e, #15) displays distinguishable lattice fringes in separate domains. Their interlayer distance corresponds well to unreacted α-Mn_2O_3, as-formed L-Zn_xMnO_2, and MnOOH phases, where the latter result from Zn^{2+} and H^+ insertion, respectively. Furthermore, the XPS O1s spectrum (Figure S17, Supporting Information) of an electrode at the same charge state (#15) reveals a substantial increase of the peak related to Mn-OH bond compared to the pristine (#1), implying the MnOOH formation.[6]

Based on the above results, we can clearly state that the electrochemical mechanism of the Zn/m-α-Mn_2O_3 cell involves Zn^{2+} and H^+ co-intercalation in the second cycle. In fact, the effect of H^+ intercalation is also obvious in the Zn/0.2 M $MnSO_4$/m-α-Mn_2O_3 cell with Zn^{2+}-free electrolyte (Figures S10 and S18, Supporting Information). As already discussed in the first cycle, due to the lack of Zn^{2+}, only a negligible capacity is delivered during the first discharge, while a measurable capacity is observed in the first charge due to birnessite (MnO_2) formation (Figure S10, Supporting Information). In the second discharge, we observe a slopy feature (Figure S18, Supporting Information with related discussion), which can be assigned to the dissolution of birnessite-MnO_2 and H^+ intercalation. Furthermore, a closer comparison of the second discharge curves of the cells with the two different electrolytes (3.0 M $ZnSO_4$ + 0.2 M $MnSO_4$ and 0.2 M $MnSO_4$, Figure S18, Supporting Information with discussion), coupled with the above-discussed results, reveals that the H^+ and Zn^{2+} intercalation reactions occur sequentially in the 3.0 M $ZnSO_4$ + 0.2 M $MnSO_4$ system in the second discharge. First, H^+ insertion occurs in the steep slope from 1.9 to ≈1.44 V, followed by mainly Zn^{2+} intercalation in the first and second plateaus. This conclusion is in good agreement to the findings obtained from the electrochemical impedance spectroscopy (EIS) analysis (Figure S19, Supporting Information with related discussion) and the investigation of the electrochemical behavior of Zn/m-α-Mn_2O_3 cells with two different electrolytes (i.e., aqueous and organic $ZnSO_4$ solution, see Figure S20, Supporting Information and related discussion).

Apart from the charge storage by Zn^{2+} and H^+ co-intercalation, the voltage profile and ex situ SEM images (#8 → #19) provide more information about the origin of the additional charge uptake. First, a tiny plateau (i.e., third one, Figure 3a) at ≈1.05 V can be observed in the second discharge curve, which we assign to the structural transformation of α-Mn_2O_3 (i.e., unreacted during the initial cycle) to L-Zn_xMnO_2, due to electrochemical Zn intercalation. This contributes to the ZHSH flake formation as well. Based on the CV results, this process also happens in the following cycles. Second, apart from recording a variation of the flake-like crystals (of ZHSH), the SEM images also illustrate the morphologic evolution of birnessite-MnO_2. The interconnected porous structure successively vanishes from the surface of the electrode during the second discharge process (Figure 3d, #8 → #12), but reappears subsequently in the fully charged state (Figure 3d, #19). This morphologic change mainly derives from a repetition of the redox process between birnessite-MnO_2 (oxidative product) and Mn^{2+} in the electrolyte (reductive product). Our finding of the reversible dissolution-deposition reaction process involving Mn^{2+} is consistent with previous reports of Liang et al. and Qiao et al.[6,23] Note that a potential reaction of birnessite-MnO_2 with Zn^{2+} and H^+ possibly also leads to the gradual vanishing of the interconnected porous structure, which needs further research in our future work. The schematic illustration of the second discharge reaction mechanism displayed in Figure 4b summarizes the above-mentioned findings. Note that in the second recharge process, the reversed behavior (apart from the irreversible structural transformation of α-Mn_2O_3) occurs.

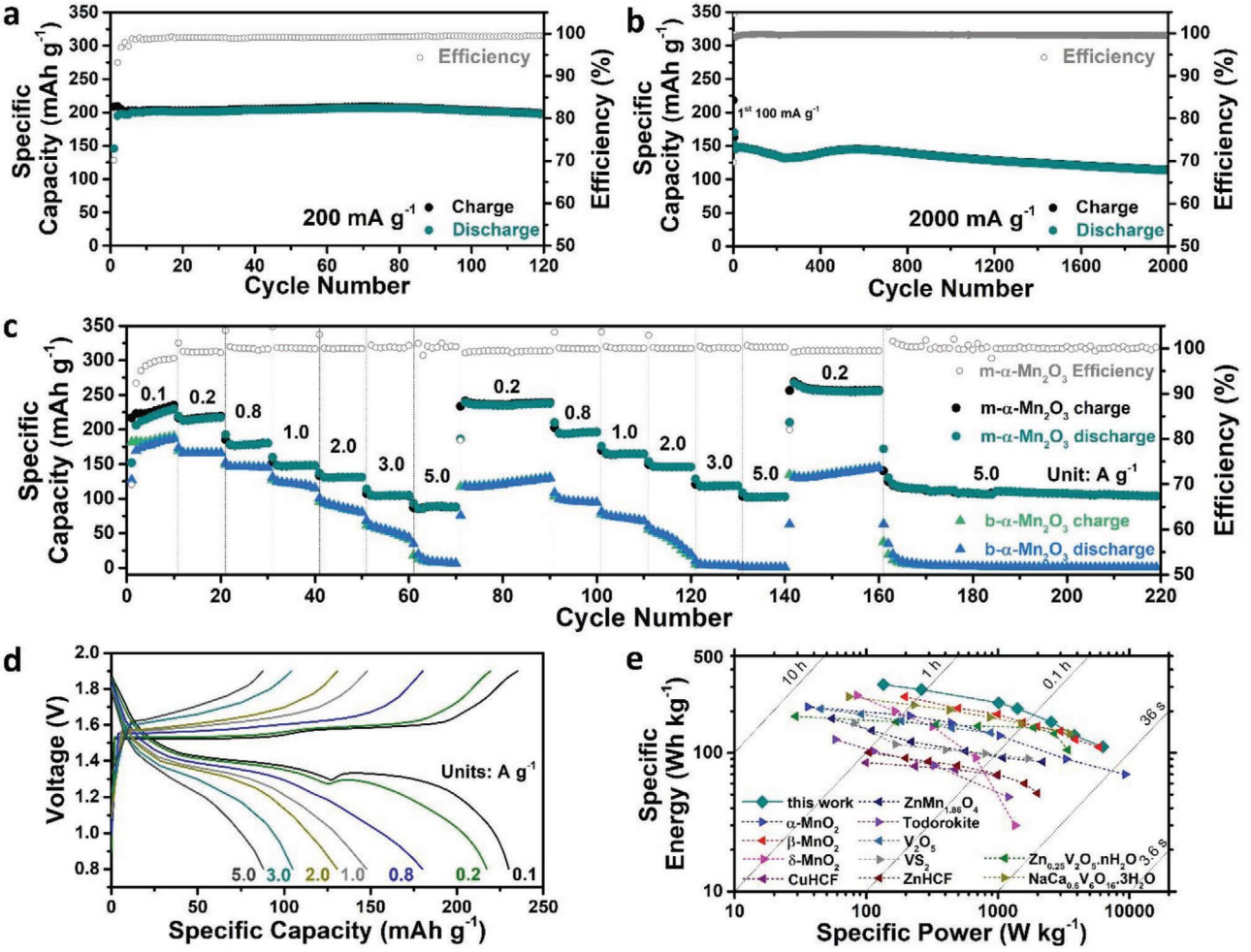

Figure 5. Electrochemical performance of Zn/m-α-Mn_2O_3 cells. Long-term cycling performance, showing the specific capacity (cyan & black) with the corresponding Coulombic efficiency (grey) versus the cycle number for a) 120 galvanostatic cycles at a constant specific current of 200 mA g^{-1} and for b) 2000 galvanostatic cycles at a constant specific current of 2000 mA g^{-1}. c) Comparison of rate capability tests of m-α-Mn_2O_3-based and b-α-Mn_2O_3-based AZMBs at different specific currents between 100 and 5000 mA g^{-1} for 220 cycles in total, with the Coulombic efficiency. d) Selected (dis-)charge voltage profiles in the first rate capability test of Zn/m-α-Mn_2O_3 cells (tenth, 20th, 30th, 40th, 50th, 60th, and 70th cycle). e) Ragone plots of Zn/m-α-Mn_2O_3 cell and AZMBs with other cathode materials reported in the literature (the values of specific energy & power for the full cell are referred to the active material amount of the cathode).

Having unraveled the complex reaction scheme contributing to charge/discharge of Zn/m-α-Mn_2O_3 cells, we focus on their electrochemical performance with a 3.0 M $ZnSO_4$ and 0.2 M $MnSO_4$ solution as electrolyte. Note that each cell contains 90 µL of electrolyte. Apart from the initial cycle, the high reversibility of the Zn/m-α-Mn_2O_3 cells is proven by the almost overlapping waves upon consecutive CV scans (Figure 2). Galvanostatic cycling experiments were conducted at different current densities, that is, 200 mA g^{-1} (**Figure 5**a) and 2000 mA g^{-1} (Figure 5b), to evaluate the long-term cycling stability and the Coulombic efficiency of Zn/m-α-Mn_2O_3 cells.

With respect to the cycling stability, Figure 5a shows that the cells possess a promising long-term cycling performance, providing 200 mAh g^{-1} after 120 cycles (i.e., ≈99% capacity retention with respect to the second cycle). Important, the Coulombic efficiency is constantly above 99% after the fifth cycle. The voltage profiles recorded during a few selected cycles (see Figure S21, Supporting Information) show a negligible discharge voltage decay over 100 cycles, with no obvious polarization appearing upon the cycling test. Furthermore, the ex situ SEM image of the m-α-Mn_2O_3 electrode after 120 cycles (Figure S22, Supporting Information) demonstrates that the original microrod structure is well retained. Also, the ex situ XRD pattern of the same sample confirms that the crystal structure of α-Mn_2O_3 is maintained (Figure S23, Supporting Information). Such an excellent cycling performance is associated with the addition of Mn^{2+} in the electrolyte, limiting the dissolution of Mn^{2+} from the electrode as well as suppressing the overreaction of m-α-Mn_2O_3 (Figure S16, Supporting Information with related discussion), and the mesoporous framework of m-α-Mn_2O_3, which can act as buffer to alleviate the volume variation during cycling.[16] It should be noted that here H_2O (including H^+) is involved in various electrochemical reactions, especially the phase transition of α-Mn_2O_3. Thus,

having sufficient electrolyte (90 µL) in the cell is necessary for achieving such an excellent performance (see Figure S24, Supporting Information with discussion). Remarkably, even upon high specific current tests (2000 mA g^{-1}; Figure 5b) the Zn/m-α-Mn_2O_3 cells exhibit a rather stable long-term behavior for over 2000 cycles, together with a Coulombic efficiency approaching 100%, from the tenth to the 2000th cycle. After 2000 cycles, the cell can still show a specific capacity of 116 mAh g^{-1}, meaning that the capacity decay is only ≈0.009% per cycle.

The rate capability of the m-α-Mn_2O_3-based and b-α-Mn_2O_3-based AZMBs was tested at various specific currents from 0.1 to 5.0 A g^{-1}. Because of the unique mesoporous structure, the Zn/m-α-Mn_2O_3 cells exhibited an impressive rate performance and cycling stability at all C rates investigated, as shown in Figure 5c (the corresponding voltage profiles are presented in Figure 5d). When tested at 0.1, 0.2, 0.8, 1.0, 2.0, and 3.0 A g^{-1}, average reversible capacities of 228, 217, 180, 148, 131, and 105 mAh g^{-1} were obtained, respectively. Even at a higher specific current of 5.0 A g^{-1}, the battery still showed an average specific capacity of 88 mAh g^{-1}. When the specific current was switched back to 0.2 A g^{-1}, a higher reversible capacity of ≈241 mAh g^{-1} was recovered in the 72nd cycle. More important, the Zn/m-α-Mn_2O_3 cells still maintained their outstanding rate capability and cycling stability in the second round of the rate capability tests. Actually, the average reversible capacities slightly increased to ≈196, 165, 146, 119, and 103 mAh g^{-1} at 0.8, 1.0, 2.0, 3.0, and 5.0 A g^{-1}, respectively. After reducing the specific current to 0.2 A g^{-1}, once again, the specific capacity slightly increased further up to 270 mAh g^{-1} for the 142nd cycle. Thus, the m-α-Mn_2O_3-based electrodes possess excellent reversibility and cycling stability even after repeated C rate cycling tests.[16,21] In stark contrast, the capacity of the Zn/b-α-Mn_2O_3 cell rapidly decreased with increasing specific current, resulting in only 79 and 40 mAh g^{-1} at 2.0 and 3.0 A g^{-1} in the first C-rate test. Even worse, the capacity in the second test dropped almost to 0 mAh g^{-1} in the 120th to 140th cycle (i.e., at 3.0 and 5.0 A g^{-1}).

The voltage profiles of both types of cells at various specific currents are compared in Figure S25, Supporting Information. At 0.1 A g^{-1}, the Zn/m-α-Mn_2O_3 cell shows a smaller voltage gap (0.27 V) between charge and discharge plateaus than the Zn/b-α-Mn_2O_3 (0.31 V). Furthermore, the Zn/b-α-Mn_2O_3 cell shows a significantly increasing polarization when increasing the applied current. The smaller polarization indicates faster reaction kinetics of the m-α-Mn_2O_3, probably due to the shorter pathways for the cationic charge carriers compared to those in b-α-Mn_2O_3.[31,32] This evidence was further demonstrated by using EIS analysis. The EIS profiles of AZMBs with m-α-Mn_2O_3 and b-α-Mn_2O_3 electrode at pristine state are displayed in Figure S26, Supporting Information, both containing the depressed semicircle in high frequency region followed by one straight line in low frequency area. Notably, the semicircle recorded for m-α-Mn_2O_3 is much smaller than that for b-α-Mn_2O_3, suggesting a lower impedance of the former and further confirming the substantially enhanced transport of cationic charge carriers within the as-fabricated mesoporous material (i.e., m-α-Mn_2O_3).[33,34] Finally, the comparison of the performance with the state-of-the-art results in previous studies on Zn/MnO_z ($1 \le z \le 2$) cells is summarized in Tables S3 and S4, Supporting Information, demonstrating the superior cycling stability and rate capability in this work with regard to recently reported works. Besides, the superior electrochemical performance is further evidenced in the Ragone plot (specific energy versus specific power at different C rates; Figure 5e), when compared with the reported α-MnO_2,[35] β-MnO_2,[9] δ-MnO_2,[36] CuHCF,[37] $ZnMn_{1.86}O_4$,[38] Todorokite,[39] V_2O_5,[40] VS_2,[41] ZnHCF,[42] $Zn_{0.25}V_2O_5.nH_2O$,[29] and $NaCa_{0.6}V_6O_{16}.3H_2O$[40] as cathode for AZMBs. High specific energy and specific power were simultaneously achieved by m-α-Mn_2O_3, that is, 311 Wh kg^{-1} at 135 W kg^{-1} and 111 Wh kg^{-1} at 6282 W kg^{-1}, respectively.

3. Conclusion

To summarize, combining different analytic techniques with galvanostatic dis-/charging in different electrolytes, we have unraveled a complex scheme of charge storage mechanism for α-Mn_2O_3 cathodes in AZMBs. This constitutes the first report that cubic α-Mn_2O_3 undergoes an irreversible phase transformation upon Zn intercalation (discharge) during the initial few cycles, coupled with the dissolution of Mn^{2+} and OH^- into the electrolyte. Finally, a layered-type L-Zn_xMnO_2 is formed that allows reversible Zn^{2+} de-/intercalation during further cycles. This reversible process goes along with a repeated dissolution-deposition of Mn^{2+} on the cathode surface and H^+ insertion/extraction along with a self-regulating process of electrolyte-assisted formation/dissolution of flake-like ZHSH. Moreover, we have demonstrated that MnO_2, derived from L-Zn_xMnO_2 and Mn^{2+} dissolved in the electrolyte, is the actual host for the intercalation of H^+, rather than the bare α-Mn_2O_3. These processes, together with the hierarchical mesoporous structure, the nanoscale particle size of α-Mn_2O_3 as well as the pre-addition of Mn^{2+} in the electrolyte, lead to a promising cycling stability of aqueous Zn/m-α-Mn_2O_3 cells with 116 mAh g^{-1} after 2000 cycles and an excellent rate capability with 103 mAh g^{-1} at 5.0 A g^{-1}, which is superior to most of the reported cathodes. While these results by themselves are already remarkable, we anticipate that the complex electrochemical reaction scheme derived here is of general relevance for AZMBs and can guide future research.

4. Experimental Section

Chemicals: Zinc sulfate heptahydrate ($ZnSO_4{\cdot}7H_2O$, 99%) was obtained from VWR LIFE SCIENCE. Manganese(II) sulfate monohydrate ($MnSO_4{\cdot}H_2O$, 99%) was purchased from Sigma Aldrich Chemical Co. Manganese (III) oxide (α-Mn_2O_3, 98%) was obtained from Alfa Aesar Chemical Co.

Preparation of m-α-Mn_2O_3 and b-α-Mn_2O_3: For m-α-Mn_2O_3, the synthesis of the Mn-based MOF precursor has been reported in the previous work.[16] The as-obtained Mn-MOF (200 mg) was annealed in a muffle furnace at 600 °C for 2 h under air atmosphere with a temperature ramp of 5 °C min^{-1}. After natural cooling, mesoporous α-Mn_2O_3 microrod material (black powder) was obtained. In addition, one-step purification treatment was performed for commercial α-Mn_2O_3, that is, annealing at 200 °C under air atmosphere for 2 h to obtain pure b-α-Mn_2O_3.

Materials Characterization: Powder XRD measurements were performed in a Bruker D8 Advance instrument, using Cu-K_α radiation

with a wavelength of 0.154 nm. Morphological, compositional, and structural information of the as-obtained samples was obtained from field-emission SEM and EDX spectroscopy using a ZEISS 1550VP. (HR-) TEM was carried out on a Cs-corrected transmission electron microscope FEI Titan (80-300) at 80 kV. The XPS measurements were performed on a PHI 5800 MultiTechnique ESCA System using monochromatic Al-K_α (1486.6 eV) radiation (250 W, 13 kV), a detection angle of 45°, and pass energies of 93.9 and 29.35 eV for survey and detail spectra, respectively. All spectra were referenced to the C1s peak of adventitious carbon, which was set to 284.8 eV for binding energy calibration. N_2 adsorption–desorption isotherms (Autosorb-iQ, Quantachrome) at 77 K were recorded to gain the BET specific surface area of the samples, and the pore size distribution of m-α-Mn_2O_3 based on the BJH method. Each sample was heated at 120 °C (24 h) for outgassing under vacuum before the measurement. TGA data of Mn-MOF precursor, m-α-Mn_2O_3, and b-α-Mn_2O_3 were collected using a thermogravimetric analyzer (TA Instruments, Model Q5000) at a heating rate of 5 °C min^{-1} under air flow. The manganese content in aqueous solution was determined via ICP-OES on both a PerkinElmer Optima 4300 DV and a Thermo Scientific iCAP 7600.

Electrochemical Characterization: The working electrodes (WEs) were composed of 80 wt% m-α-Mn_2O_3 or b-α-Mn_2O_3, 10 wt% SuperC65 (TIMCAL) as conductive carbon, and 10 wt% polyvinylidene fluoride (PVdF) as binder. To prepare the WEs, a 10 wt% solution was first obtained by dissolving the PVdF powder into N-methylpyrrolidone (NMP, Sigma Aldrich) solvent. Then, the powders of m-α-Mn_2O_3/b-α-Mn_2O_3 and SuperC65 were added to the PVdF-based solution, and subsequently stirred overnight to form the slurry. The resulting black slurry was coated onto a stainless-steel foil (Goodfellow) by doctor blading with a wet film thickness of 200 µm. The as-obtained electrodes were first dried in an oven at 60 °C overnight, then punched into disks with 14 mm diameter and vacuum-dried for 24 h at 120 °C. The mass loading of the active materials was 1.43–1.62 mg cm^{-2}. The electrochemical performance of the as-prepared electrodes was measured in galvanostatic (dis-)charge experiments, employing stainless steel 2032 coin cells with a Zn foil (Goodfellow, >99.99%) as counter electrode. Conversely, CV and EIS measurements of the m-α-Mn_2O_3/b-α-Mn_2O_3 cathode were performed in a three-electrode cell (Swagelok-type setup) with zinc foil as reference and counter electrode. In both setups, a glass fiber film disk (Whatman GF/F) was used as separator, which was soaked by five different kinds of electrolyte, viz., 3.0 M $ZnSO_4$ aqueous solution with 0.2 M $MnSO_4$ as additive, 3.0 M $ZnSO_4$ aqueous solution, 0.2 M $MnSO_4$ aqueous solution, 3.5 M $MnSO_4$ aqueous solution, and 3.0 M $ZnSO_4$ DMSO solution. The AZMB was assembled under air atmosphere before the electrolyte was de-aerated by bubbling nitrogen for 1 h. All electrochemical measurements were carried out at 20 ± 2 °C. The galvanostatic (dis-)charge experiments were performed using a Maccor 3000 battery tester in the voltage range 0.8–1.9 V. The CV measurements were conducted with a VMP3 potentiostat (Biologic Science Instruments) in the same potential range, that is, 0.8–1.9 V versus Zn/Zn^{2+}. The EIS experiments were performed with the same instrument, in the frequency range from 1 MHz to 10 mHz with a sinusoidal signal amplitude of 5 mV. For ex situ characterization, the test cells were disassembled in an Ar-filled glovebox in order to avoid electrode contamination. As-collected electrodes were naturally dried at ambient temperature in the Ar-filled glovebox before XRD, SEM, and TEM studies. For XPS measurements, as-collected electrodes were rinsed with deionized water, which was de-aerated by bubbling nitrogen for 1 h before using. Then electrodes were naturally dried under ambient temperature in the Ar-filled glovebox before transfer in Ar atmosphere to the sample load lock of the XPS system.

Supporting Information

Supporting Information is available from the Wiley Online Library or from the author.

Acknowledgements

Y.M., Y.-J.M., K.-C.C., and X.L. gratefully acknowledge financial support from the Chinese Scholarship Council. Financial support from the Helmholtz Association is also acknowledged. Moreover, the authors would like to thank Dr. Yuanchun Ji for TEM testing. This work contributes to the research performed at CELEST (Center for Electrochemical Energy Storage Ulm-Karlsruhe).

Open access funding enabled and organized by Projekt DEAL.

Conflict of Interest

The authors declare no conflict of interest.

Data Availability Statement

Research data are not shared.

Keywords

α-Mn_2O_3, aqueous zinc-metal batteries, cathodes, energy storage mechanisms, hierarchical mesoporous structures

Received: March 24, 2021
Revised: July 1, 2021
Published online:

[1] X. Jia, C. Liu, Z. G. Neale, J. Yang, G. Cao, *Chem. Rev.* **2020**, *120*, 7795.
[2] H. Zhang, X. Liu, H. Li, I. Hasa, S. Passerini, *Angew. Chem., Int. Ed.* **2021**, *60*, 598.
[3] G. Fang, J. Zhou, A. Pan, S. Liang, *ACS Energy Lett.* **2018**, *3*, 2480.
[4] H. Zhang, X. Liu, H. Li, B. Qin, S. Passerini, *ACS Appl. Mater. Interfaces* **2020**, *12*, 15305.
[5] C. Xia, J. Guo, P. Li, X. Zhang, H. N. Alshareef, *Angew. Chem., Int. Ed.* **2018**, *57*, 3943.
[6] D. Chao, W. Zhou, C. Ye, Q. Zhang, Y. Chen, L. Gu, K. Davey, S. Qiao, *Angew. Chem.* **2019**, *131*, 7905.
[7] Y. Zhao, Y. Zhu, X. Zhang, *InfoMat* **2020**, *2*, 237.
[8] D. Selvakumaran, A. Pan, S. Liang, G. Cao, *J. Mater. Chem. A* **2019**, *7*, 18209.
[9] N. Zhang, F. Cheng, J. Liu, L. Wang, X. Long, X. Liu, F. Li, J. Chen, *Nat. Commun.* **2017**, *8*, 405.
[10] J. Wang, J.-G. Wang, H. Liu, Z. You, C. Wei, F. Kang, *J. Power Sources* **2019**, *438*, 226951.
[11] B. Jiang, C. Xu, C. Wu, L. Dong, J. Li, F. Kang, *Electrochim. Acta* **2017**, *229*, 422.
[12] N. Liu, X. Wu, Y. Yin, A. Chen, C. Zhao, Z. Guo, L. Fan, N. Zhang, *ACS Appl. Mater. Interfaces* **2020**, *12*, 28199.
[13] D. Feng, T.-N. Gao, L. Zhang, B. Guo, S. Song, Z.-A. Qiao, S. Dai, *Nano-Micro Lett.* **2020**, *12*, 14.
[14] D. Zhang, J. Cao, X. Zhang, N. Insin, S. Wang, J. Han, Y. Zhao, J. Qin, Y. Huang, *Adv. Funct. Mater.* **2021**, *31*, 2009412.
[15] J. Long, F. Yang, J. Cuan, J. Wu, Z. Yang, H. Jiang, R. Song, W. Song, J. Mao, Z. Guo, *ACS Appl. Mater. Interfaces* **2020**, *12*, 32526.
[16] Y. Ma, Y. Ma, G. Kim, T. Diemant, R. J. Behm, D. Geiger, U. Kaiser, A. Varzi, S. Passerini, *Adv. Energy Mater.* **2019**, *9*, 1902077.
[17] G. Tian, Z. Zhao, A. Sarapulova, C. Das, L. Zhu, S. Liu, A. Missiul, E. Welter, J. Maibach, S. Dsoke, *J. Mater. Chem. A* **2019**, *7*, 15640.
[18] M. A. Stranick, *Surf. Sci. Spectra* **1999**, *6*, 39.

[19] M. Oku, K. Hirokawa, S. Ikeda, *J. Electron Spectrosc. Relat. Phenom.* **1975**, *7*, 465.
[20] Y. Ma, Y. Ma, D. Geiger, U. Kaiser, H. Zhang, G.-T. Kim, T. Diemant, R. J. Behm, A. Varzi, S. Passerini, *Nano Energy* **2017**, *42*, 341.
[21] Y. Ma, Y. Ma, D. Bresser, Y. Ji, D. Geiger, U. Kaiser, C. Streb, A. Varzi, S. Passerini, *ACS Nano* **2018**, *12*, 7220.
[22] J. Huang, Z. Wang, M. Hou, X. Dong, Y. Liu, Y. Wang, Y. Xia, *Nat. Commun.* **2018**, *9*, 2906.
[23] X. Guo, J. Zhou, C. Bai, X. Li, G. Fang, S. Liang, *Mater. Today Energy* **2020**, *16*, 100396.
[24] H. Pan, Y. Shao, P. Yan, Y. Cheng, K. S. Han, Z. Nie, C. Wang, J. Yang, X. Li, P. Bhattacharya, K. T. Mueller, J. Liu, *Nat. Energy* **2016**, *1*, 16039.
[25] M. H. Alfaruqi, V. Mathew, J. Gim, S. Kim, J. Song, J. P. Baboo, S. H. Choi, J. Kim, *Chem. Mater.* **2015**, *27*, 3609.
[26] K. Ramesh, L. Chen, F. Chen, Y. Liu, Z. Wang, Y.-F. Han, *Catal. Today* **2008**, *131*, 477.
[27] Q. Tang, L. Jiang, J. Liu, S. Wang, G. Sun, *ACS Catal.* **2014**, *4*, 457.
[28] H. W. Nesbitt, D. Banerjee, *Am. Mineral.* **1998**, *83*, 305.
[29] D. Kundu, B. D. Adams, V. Duffort, S. H. Vajargah, L. F. Nazar, *Nat. Energy* **2016**, *1*, 16119.
[30] S. Tepavcevic, H. Xiong, V. R. Stamenkovic, X. Zuo, M. Balasubramanian, V. B. Prakapenka, C. S. Johnson, T. Rajh, *ACS Nano* **2012**, *6*, 530.
[31] L. Chen, Z. Yang, F. Cui, J. Meng, Y. Jiang, J. Long, X. Zeng, *Mater. Chem. Front.* **2020**, *4*, 213.
[32] Y. Fu, Q. Wei, G. Zhang, X. Wang, J. Zhang, Y. Hu, D. Wang, L. Zuin, T. Zhou, Y. Wu, S. Sun, *Adv. Energy Mater.* **2018**, *8*, 1801445.
[33] Y. Zheng, T. Zhou, C. Zhang, J. Mao, H. Liu, Z. Guo, *Angew. Chem., Int. Ed.* **2016**, *55*, 3408.
[34] Y. Ma, Y. Ma, T. Diemant, K. Cao, U. Kaiser, R. J. Behm, A. Varzi, S. Passerini, *ChemElectroChem* **2021**, *8*, 918.
[35] C. Xu, B. Li, H. Du, F. Kang, *Angew. Chem., Int. Ed.* **2012**, *51*, 933.
[36] M. H. Alfaruqi, J. Gim, S. Kim, J. Song, D. T. Pham, J. Jo, Z. Xiu, V. Mathew, J. Kim, *Electrochem. Commun.* **2015**, *60*, 121.
[37] R. Trócoli, F. La Mantia, *ChemSusChem* **2015**, *8*, 481.
[38] N. Zhang, F. Cheng, Y. Liu, Q. Zhao, K. Lei, C. Chen, X. Liu, J. Chen, *J. Am. Chem. Soc.* **2016**, *138*, 12894.
[39] J. Lee, J. B. Ju, W. I. Cho, B. W. Cho, S. H. Oh, *Electrochim. Acta* **2013**, *112*, 138.
[40] K. Zhu, T. Wu, K. Huang, *Adv. Energy Mater.* **2019**, *9*, 1901968.
[41] P. He, M. Yan, G. Zhang, R. Sun, L. Chen, Q. An, L. Mai, *Adv. Energy Mater.* **2017**, *7*, 1601920.
[42] L. Zhang, L. Chen, X. Zhou, Z. Liu, *Adv. Energy Mater.* **2015**, *5*, 1400930.